

# A 2- $\mu\text{m}$ BiCMOS Rectifier-Free AC–DC Piezoelectric Energy Harvester–Charger IC

Dongwon Kwon, *Graduate Student Member, IEEE*, and Gabriel A. Rincón-Mora, *Senior Member, IEEE*

**Abstract**—A fundamental problem that miniaturized systems like biomedical implants face is limited space for storing energy, which translates to short operational life. Harvesting energy from the surrounding environment, which is virtually a boundless source at these scales, can overcome this restriction, if losses in the system are sufficiently low. To that end, the 2- $\mu\text{m}$  BiCMOS switched-inductor piezoelectric harvester prototype evaluated and presented in this paper eliminates the restrictions associated with a rectifier to produce and channel 30  $\mu\text{W}$  from a periodic 72- $\mu\text{W}$  piezoelectric source into a battery directly. In doing so, the circuit also increases the system's electrical damping force to draw more power and energy from the transducer, effectively increasing its mechanical-electrical efficiency by up to 78%. The system also harnesses up to 659 nJ from non-periodic mechanical vibrations, which are more prevalent in the environment, with  $6.1 \pm 1.5\%$  to  $8.8 \pm 6.9\%$  of end-to-end mechanical-electrical efficiency.

**Index Terms**—Energy harvesting, vibration, piezoelectric, wireless microsensor, biomedical implant, body-sensor network, battery charger, rectifier-free, harvester, switched-inductor converter.

## I. PIEZOELECTRIC ENERGY HARVESTERS

MINIATURIZED mobile electronic systems, such as biomedical drug-delivery implants [1], acceleration- and pressure-monitoring sensors [2]–[3], and microsensor nodes in body-sensor networks [4]–[5], have so little space for energy storage that they suffer from short operational lives. Unfortunately, replacing easily exhaustible onboard batteries is prohibitive because the systems often conduct *in situ* measurements in unreachable places, like in the human body, and operate in concert with numerous other devices [5], where the personnel, risks, and logistical costs of maintaining *all* batteries charged are unacceptably high. Harvesting energy, however, from light [6], heat [7]–[8], radiation [9], and motion [10]–[12] is an attractive, though not easy alternative for replenishing small batteries and capacitors.

Although the application ultimately determines what energy source suits best, harvesting kinetic energy is promising because motion and vibrations are abundant (in the ankle, for example) and produce moderate power levels. For context, solar light generates more power, but only when exposed

directly to the sun, and power densities derived from indoor lighting, thermal gradients, and radio-frequency (RF) waves fall well below their kinetic counterparts [11]–[12], although not all motion-based transducers perform equally well. Piezoelectric devices, in fact, when constrained to small platforms, generate more power than variable (electrostatic) capacitors and moving (electromagnetic) coils [11]–[13].

When considering a piezoelectric source, as shown in Fig. 1, the internal charge configuration of the material changes (much like an ac current source) to generate an alternating voltage across the equivalent capacitance that its opposing surfaces present [13]. The harvester circuit must therefore extract energy from the changing voltages of the piezoelectric capacitor and deposit charge into an energy-storage device. Because harvested power is low and uncorrelated to the load, a small battery or capacitor serves as the reservoir from which electrical functions in the system draw power on demand.

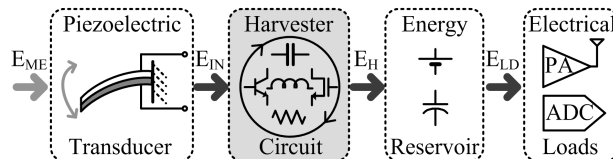


Fig. 1. Harvesting mechanical energy from piezoelectric transducers.

Conventional approaches first rectify the incoming ac voltage with a diode bridge. [14]–[15] reduce the voltage (and therefore power losses) across the pn-junction diodes by using MOS switches and driving them with a comparator that senses and ensures only small positive terminal voltages allow the switches to close. Unfortunately, input voltages must nonetheless exceed their rectified outputs for the MOS switches to conduct, which means rectifiers inevitably place a threshold limit on the mechanical input. In other words, rectified harvesters only harvest energy above a minimum input level, so they cannot extract all the energy the piezoelectric material offers. Although [16]–[20] extract more energy from the environment by boosting the transducer's electrical damping force with higher (LC-induced) piezoelectric voltages, the subsequent rectifier still suffers from a threshold minimum below which the harvester cannot harness energy. Furthermore, drawing maximum power requires an optimal rectified output voltage, so [21]–[22], at the cost of power, employ a correcting feedback loop that senses the harvester's output current to set the optimal rectified level.

A minimum threshold imposed by rectifiers is ultimately a significant fundamental limit under micro-scale dimensions because (i) miniaturized piezoelectric transducers, by default,

Manuscript received June 11, 2010. Linear Technology Corporation sponsored this research and fabricated the IC prototypes tested.

D. Kwon and G.A. Rincón-Mora are with Georgia Tech Analog, Power, and Energy IC Research Lab, School of Electrical and Computer Engineering, Georgia Institute of Technology, Atlanta, GA 30332 USA (e-mail: dkwon3@gatech.edu, Rincon-Mora@gatech.edu).

generate low voltages [23]–[26] and (ii) weak vibrations, which also produce low power, are prevalent in the environment. The underlying aim of the proposed harvester is to eliminate the rectifier and its resulting low-voltage limitation. Another important advantage of the circuit is that it augments, like [16]–[20] but without a rectifier, the electrical damping force that it presents to the transducer to induce the system to draw more energy from the environment, effectively increasing the mechanical-electrical (and end-to-end) efficiency of the transducer (and system). To that end, while [27] presented the simulation results of the proposed power stage and [28] briefly reported partial experimental performance from the prototyped power stage and its control circuit, Section II of this paper details how the prototype system operates across a cycle and how it induces the transducer to harness more energy from the environment. Section III then describes in depth the integrated circuit (IC) implementation and Sections IV and V illustrate the charging and efficiency performance of the prototype with both periodic and non-periodic mechanical inputs (i.e., vibrations), drawing relevant conclusions in Section VI.

## II. PROPOSED HARVESTER-CHARGER SYSTEM

### A. Energy Flow

Fig. 2 graphically illustrates how the proposed harvester operates and transfers energy across a vibration cycle. When vibrations move the piezoelectric cantilever in the positive cycle, for example, the system waits until the voltage across piezoelectric capacitance  $C_{PZT}$  peaks, which happens when the transducer's cantilever reaches its maximum displacement. At this point, the system energizes harvesting inductor  $L_H$  from  $C_{PZT}$  in energizing time  $\tau_{LE}^+$  and then de-energizes  $L_H$  into the battery in de-energizing time  $\tau_{LDE}^+$ . Transferring energy this way only requires a few microseconds, which represents a negligible fraction of the millisecond vibration period, so the position of the transducer is, for all practical purposes, static during the transfer. Similarly, after depositing positive-cycle charge into the battery, the system waits until the piezoelectric device charges  $C_{PZT}$  in the negative direction to its negative peak. The switched-inductor circuit then quickly energizes and de-energizes  $L_H$  in  $\tau_{LE}^-$  and  $\tau_{LDE}^-$  from  $C_{PZT}$  to the battery. This negative-cycle transfer concludes the cycle, and the sequence repeats as long as vibrations persist.

$C_{PZT}$  stores the energy that the piezoelectric material produces each half cycle ( $E_{IN}^+$ ) and the switched-inductor converter extracts  $E_{IN}^+$  from  $C_{PZT}$  to reset  $C_{PZT}$ 's voltage  $v_{PZT}$  to 0 V. Assuming piezoelectric current  $i_{PZT}$  is sinusoidal at  $I_{PZT}\sin(\omega_{VIB}t)$ ,  $v_{PZT}$  during the positive-cycle time  $\tau_{CE}^+$  is

$$v_{PZT}(t) = \frac{1}{C_{PZT}} \int_0^t i_{PZT}(\tau) d\tau = \left( \frac{I_{PZT}}{\omega_{VIB} C_{PZT}} \right) [1 - \cos(\omega_{VIB}t)] \quad (1)$$

Therefore, after  $\tau_{CE}^+$ ,  $C_{PZT}$  accumulates

$$E_{IN}^+ \approx \int_0^{\tau_{CE}^+=T/2} i_{PZT}(t) v_{PZT}(t) dt = \frac{2I_{PZT}^2}{\omega_{VIB}^2 C_{PZT}} \quad (2)$$

Since the negative cycle generates an equivalent amount (i.e.,  $E_{IN}^+ \approx E_{IN}^-$ ), the system harnesses  $4I_{PZT}^2/\omega_{VIB}^2 C_{PZT}$  from each

vibration period, which is four times ( $4\times$ ) more energy than the ideal diode-rectified case can possibly induce [21].

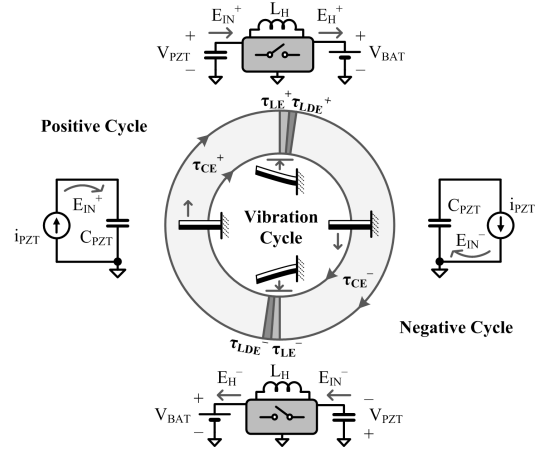


Fig. 2. Full-cycle operation of the proposed piezoelectric harvester.

### B. Time-Domain Operation

In the positive cycle, with switch  $S_1$  open, the switched-inductor power stage in Fig. 3 waits for  $i_{PZT}$  to charge  $C_{PZT}$  to peak positive voltage  $V_{PZT(PK)}^+$ , as the experimental waveforms of Fig. 4 illustrate.  $V_{PZT(PK)}^+$  is not the actual peak because the implemented circuit includes delay and offset, the causes and implications of which subsequent subsections will address. The controller then closes  $S_1$  and  $S_N$  to energize  $L_H$  from  $C_{PZT}$  for energizing time  $\tau_{LE}^+$ , allowing  $L_H$ 's current  $i_L$  to reach positive peak current  $I_{L(PK)}^+$ . Because a capacitor fully discharges into an inductor in a quarter of its LC resonance period, the system sets  $\tau_{LE}^+$  to one-fourth of  $2\pi\sqrt{L_H C_{PZT}}$ . After  $\tau_{LE}^+$ ,  $S_N$  opens and  $i_L$  charges the parasitic capacitance at  $v_{SW}^+$  until non-inverting diode  $D_N$  forward biases and steers  $i_L$ 's de-energizing (battery) current  $i_{BAT}^+$  into the battery. Once  $D_N$  completely drains  $L_H$ , after de-energizing time  $\tau_{LDE}^+$ ,  $D_N$  opens automatically (i.e., asynchronously).

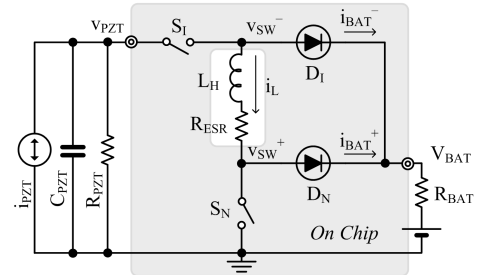


Fig. 3. Simplified schematic of the switched-inductor power stage.

The negative cycle operates similarly, except the power stage inverts its functionality to realize an inverting buck-boost translation. As such, the system waits for  $i_{PZT}$  to charge  $C_{PZT}$  in the negative direction until  $v_{PZT}$  reaches negative peak voltage  $V_{PZT(PK)}^-$ . (Like before,  $V_{PZT(PK)}^-$  is not accurate because of non-idealities in the circuit.)  $S_1$  and  $S_N$  then discharge  $C_{PZT}$  into  $L_H$  for one-fourth of  $L_H$ - $C_{PZT}$ 's resonance period, after which point  $S_1$  opens and  $i_L$  charges  $v_{SW}^-$ 's parasitic capacitance until inverting diode  $D_1$  forward biases and conducts  $i_L$ 's de-energizing (battery) current  $i_{BAT}^-$

into the battery.

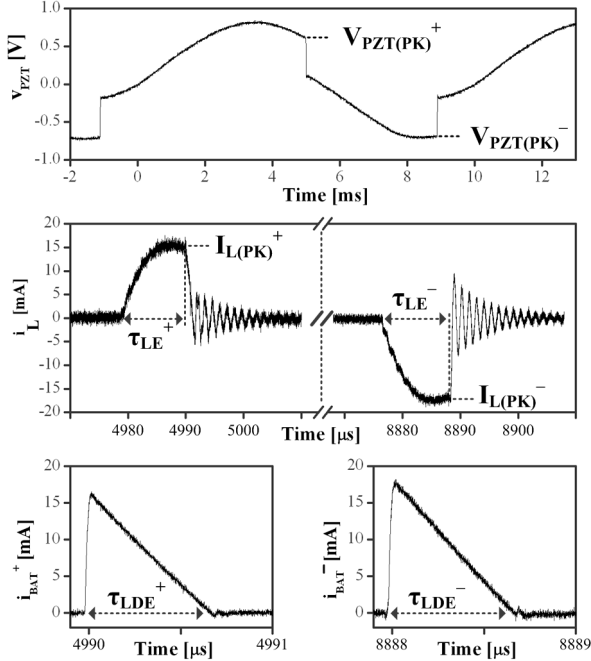


Fig. 4. Experimental time-domain waveforms of piezoelectric voltage  $v_{PZT}$ , inductor current  $i_L$ , and the de-energizing (battery) currents  $i_{BAT}^+$  and  $i_{BAT}^-$ .

Unlike rectifier-based harvesters, the proposed switched-inductor circuit can de-energize (and therefore harness) *all* piezoelectric energy in  $C_{PZT}$ , which is to say the circuit does not suffer from a minimum input threshold. What is more,  $L_H$  automatically raises  $v_{SW}^+$  and  $v_{SW}^-$  to whatever voltage the battery demands, which means the circuit does not require the additional dc-dc converter stage that [20]–[22] use to drive charge into the battery. Unlike the converters in [21]–[22], which include a lossy feedback loop to adjust the rectifier output voltage to draw the maximum power from  $C_{PZT}$ , the proposed harvester can derive four times ( $4\times$ ) more energy than rectified harvesters without a correcting loop.

### III. INTEGRATED-CIRCUIT DESIGN

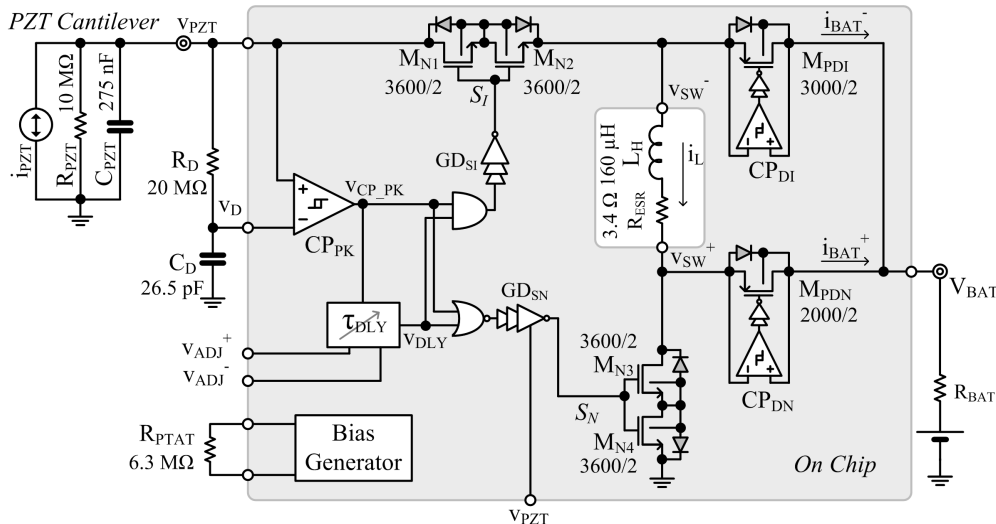


Fig. 5. Prototyped piezoelectric energy harvester IC (in gray) and system (transistor dimensions are in  $\mu\text{m}$ ).

The prototyped harvester shown in Fig. 5 integrates the switches, controller, and bias generator into a single  $2\text{-}\mu\text{m}$  BiCMOS IC. Bias resistor  $R_{PTAT}$  and delay filter elements  $R_D$  and  $C_D$  are off chip for testing flexibility. For the same reasons, external voltages  $v_{ADJ}^+$  and  $v_{ADJ}^-$  adjust energizing times  $\tau_{LE}^+$  and  $\tau_{LE}^-$  externally. The piezoelectric cantilever, the battery, and  $L_H$  are also off chip.

#### A. Switches and Gate Drivers

A series combination of two NMOS transistors in an isolated p-well implements both  $S_I$  and  $S_N$  in Fig. 5. The purpose of the back-to-back body diodes is to block the undesired diode current that would otherwise result through the body diode of a single transistor when  $v_{PZT}$  swings below ground (in the negative cycle) or above battery voltage  $V_{BAT}$  (in the positive cycle). Note that the series combination of two switches increases channel resistance and gate capacitance, which raise conduction and switching losses, respectively, but not to the extent body-diode conduction would dissipate power.

Allowing  $v_{PZT}$  to swing below ground demands that  $S_N$ 's gate driver  $GD_{SN}$  outputs a negative voltage. The reason for this is that, while  $S_N$  is open during the negative cycle, when  $v_{PZT}$  falls below ground,  $S_I$  remains closed and, as a result, switch-node voltages  $v_{SW}^+$  and  $v_{SW}^-$  follow  $v_{PZT}$  below ground. During this time, driving  $S_N$ 's gate to zero would not disengage  $S_N$ . To avoid this problem,  $GD_{SN}$ 's last inverter stage connects to  $v_{PZT}$  instead of ground, as Fig. 6a shows. Accordingly, as the simulation results of Fig. 6b illustrate,  $GD_{SN}$ 's output  $v_{GDSN\_OUT}$  follows  $v_{PZT}$  during the negative cycle and nears  $V_{BAT}$  otherwise. Because  $S_N$ 's gate capacitance is orders of magnitude below  $C_{PZT}$ 's,  $GD_{SN}$  hardly drains  $C_{PZT}$ , that is, has negligible impact on  $v_{PZT}$ . However, when the system raises  $v_{GDSN\_OUT}$  to  $V_{BAT}$  (to close  $S_N$  and energize  $L_H$ ), inverter  $M_{PGD3}\text{-}M_{NGD3}$  conducts considerable shoot-through current (for about 50 ns) because  $M_{NGD3}$ 's source voltage  $v_{PZT}$  rises more slowly (in  $\tau_{LE}^-$ ) than  $M_{NGD3}$ 's gate voltage drops to zero (in a few ns). To minimize this loss,  $M_{NGD3}$ 's width-length aspect ratio  $W/L$  is relatively low to increase resistance, yet high enough to open  $S_N$  in time to drain  $L_H$  into the battery

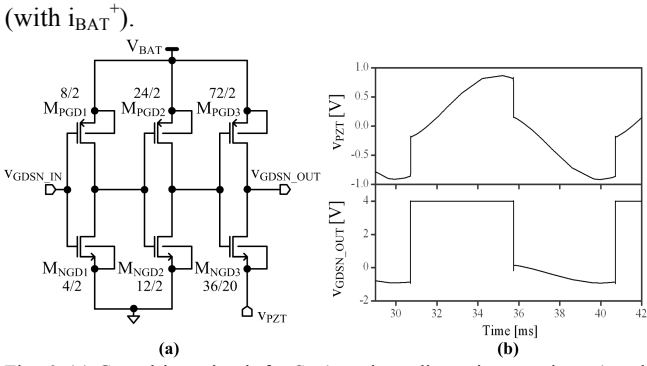


Fig. 6. (a) Gate-driver circuit for  $S_N$  (transistor dimensions are in  $\mu\text{m}$ ) and (b) the simulated waveforms of  $v_{PZT}$  and the gate voltage of  $S_N$  ( $V_{GDSN\_OUT}$ ).

### B. Self-synchronizing Switches

To reduce the diode-voltage conduction loss across battery-charging diodes  $D_N$  and  $D_I$  in the power stage of Fig. 3, the prototyped harvester in Fig. 5 replaces them with low-drop synchronous MOS switches  $M_{PDN}$  and  $M_{PDI}$ . Here, comparators  $CP_{DN}$  and  $CP_{DI}$  sense when  $D_N$  and  $D_I$ 's anode (switching) voltages  $v_{SW}^+$  and  $v_{SW}^-$  just surpass their cathode counterpart  $V_{BAT}$  to engage  $M_{PDN}$  and  $M_{PDI}$ , and switch them off otherwise.  $CP_{DN}$  and  $CP_{DI}$  must therefore (i) respond quickly (to reduce the time the lossy body-diodes conduct charging currents and keep  $M_{PDN}$  and  $M_{PDI}$  from draining the battery with negative current) and (ii) dissipate little energy [29]–[31].

A fast response implies considerable quiescent current and low energy means the comparators must operate only when needed (asynchronously): when  $L_H$  drains  $i_L$  into the battery (during  $\tau_{LDE}^+$  and  $\tau_{LDE}^-$ ). Fortunately,  $\tau_{LDE}^+$  and  $\tau_{LDE}^-$  are a small fraction of the vibration period so energy remains low (at 0.5 nJ per cycle in the prototyped case). Considering that, the comparator in Fig. 7a powers only when  $i_L$  is non-zero and the corresponding switching (anode) voltage  $v_{SW}$  is well above zero (above  $M_{PB}$  and  $M_{NB}$ 's combined gate-source voltages), which only happens when  $L_H$  is ready to charge the battery. During that time, some of  $i_L$  (as limited by  $R_{BIAS}$ ) flows into bias mirror  $M_{NB}$ - $M_{NO}$  to establish a threshold current about which  $M_{PO}$  determines the state of the comparator. That way, since  $M_{PB}$  and  $M_{PO}$  match,  $M_{PO}$  conducts less current and engages  $M_{PDN}$  (or  $M_{PDI}$ ) when  $V_{BAT}$  is below  $v_{SW}$ , and *vice versa* otherwise.

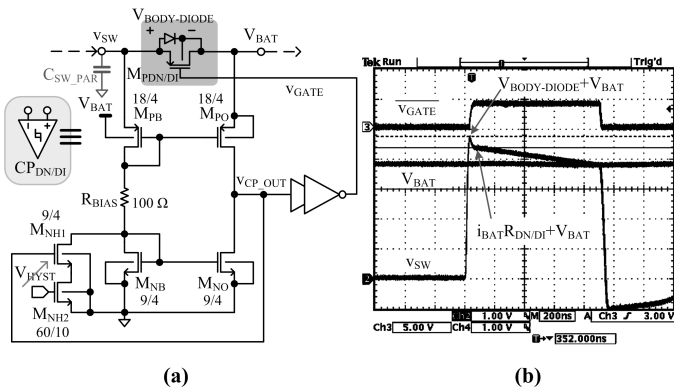


Fig. 7. (a) Schematic (transistor dimensions are in  $\mu\text{m}$ ) and (b) experimental waveforms of the self-synchronizing switches.

Because the comparator does not draw current until  $v_{SW}$  rises well above ground,  $i_L$  charges  $v_{SW}$ 's parasitic capacitance  $C_{SW\_PAR}$  quickly, as Fig. 7b's experimental waveform shows, and  $M_{NO}$  sinks sufficient current to ensure  $v_{CP\_OUT}$  transitions low quickly (to engage  $M_{PDN}$  or  $M_{PDI}$ ). Note  $M_{PDN}$ 's (or  $M_{PDI}$ 's) body diode conducts current while the comparator reacts to close  $M_{PDN}$  (or  $M_{PDI}$ ). Once engaged,  $v_{SW}$  remains above  $V_{BAT}$  by the Ohmic voltage  $i_L$  produces across  $M_{PDN}$ 's (or  $M_{PDI}$ 's) series resistance. As a result,  $v_{SW}$  decreases with  $L_H$ 's falling  $i_L$ , as  $L_H$  de-energizes. When  $i_L$  reaches zero, which happens when the system exhausts  $L_H$ 's energy,  $v_{SW}$  falls to  $V_{BAT}$  and the comparator transitions to disengage  $M_{PDN}$  (or  $M_{PDI}$ ). Because  $i_L$  no longer carries sufficient current to power the comparator, the circuit shuts down automatically.

During the turn-off transition, the comparator receives a small overdrive voltage so its shut-off time is longer than its counterpart is. As a result, while still closed,  $M_{PDN}$ 's (or  $M_{PDI}$ 's) reverse current can not only discharge the battery but also dissipate power. To prevent this reverse current, the comparator shifts the shut-off trip-point up to transition earlier (when  $v_{SW}$  is slightly above  $V_{BAT}$ ) by leaking current away from  $M_{NB}$  through  $M_{NH1}$ . The positive feedback that  $M_{NH1}$  creates engages only after  $v_{CP\_OUT}$  rises above ground by more than  $M_{NH1}$ 's  $V_{TN}$ , which happens after the comparator decides to raise  $v_{CP\_OUT}$ . In other words,  $M_{NH1}$  accelerates the circuit only after it begins to trip.  $M_{NH1}$  also imbalances gate-coupled pair  $M_{PB}$ - $M_{PO}$  with  $M_{NH2}$ 's current to offset  $v_{SW}$ 's rising trip-point (and create a hysteresis) that helps in preventing transient and ringing events in  $v_{SW}$  from asserting inadvertent transitions in the comparator. (In the prototype system of Fig. 7a,  $V_{HYST}$  sets  $M_{NH2}$ 's current.)

### C. Control Circuit

The purpose of the control block is to determine when to start and stop energizing  $L_H$ . First,  $S_I$  and  $S_N$  should start discharging  $C_{PZT}$  into  $L_H$  when  $v_{PZT}$  peaks. To this end, comparator  $CP_{PK}$  in Fig. 5 compares  $v_{PZT}$  with a delayed version of itself ( $v_D$ ) to capture the moments when  $v_{PZT}$  stops leading  $v_D$ . That is to say,  $v_{PZT}$  drops below  $v_D$  when  $v_{PZT}$  just begins falling from its positive peak and  $v_{PZT}$  rises above  $v_D$  when  $v_{PZT}$  just begins increasing from its negative peak.

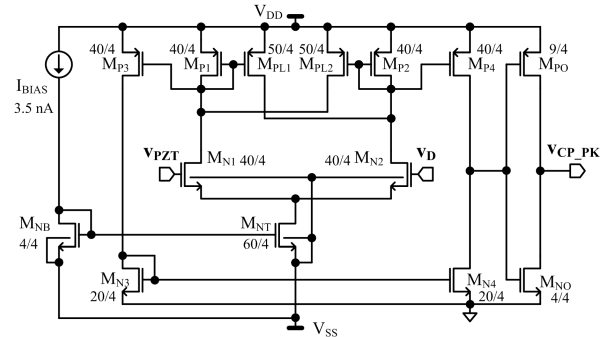


Fig. 8. Peak-detecting comparator  $CP_{PK}$  (dimensions are in  $\mu\text{m}$  and body terminals connect to their respective supplies, unless otherwise specified).

$CP_{PK}$  in Fig. 8 incorporates about  $\pm 10$  mV of hysteresis to deglitch noise in  $v_{PZT}$  and  $v_D$ . The cross-coupled, positive-feedback p-type mirror load unbalances the n-type

differential pair in both directions for that purpose. The circuit operates in subthreshold to minimize power (with nanoamps) so its delay is on the microsecond range. Such a slow response is tolerable because microseconds constitute a negligible fraction of the millisecond vibration period, meaning  $v_{PZT}$  does not change appreciably in microseconds. To mitigate risk in evaluating the power stage and its basic control scheme, external negative source  $V_{SS}$  extends  $CP_{PK}$ 's input common-mode range (ICMR) below ground so it can accommodate negative  $v_{PZT}$  voltages.

Ideally, the harvester should stop energizing  $L_H$  after one-fourth of  $L_H$ - $CP_{ZT}$ 's resonance period, after energizing periods  $\tau_{LE}^+$  and  $\tau_{LE}^-$ . For that,  $v_{ADJ}^+$ - $R_{ADJ}^+$  and  $v_{ADJ}^-$ - $R_{ADJ}^-$  in Fig. 9a set the source and sink currents that charge and discharge  $C_{ADJ}$  so that  $C_{ADJ}$ 's voltage reaches the threshold of the ensuing inverter in  $1/2\pi\sqrt{L_H CP_{ZT}}$ . Since tolerance in  $R_{ADJ}$  and  $C_{ADJ}$  offset this time, and other parasitic effects similarly shift how long  $CP_{ZT}$  should discharge into  $L_H$ ,  $v_{ADJ}^+$  and  $v_{ADJ}^-$  are adjustable (and off chip for testing flexibility). Notice  $M_{NSQ}$  and  $M_{PSQ}$  dissipate shoot-through power because  $C_{ADJ}$ 's voltage rises and falls at relatively low rates, so to reduce this loss, their channel lengths are relatively long at 10  $\mu\text{m}$ . In the case tuning the effective R-C time constants externally is prohibitive, monitoring  $L_H$ 's voltage  $v_L$  with a comparator so that it trips when  $v_L$  (which equals  $L_H di_L/dt$ ) crosses zero (when  $i_L$  peaks) can alternately set  $L_H$ 's energizing times  $\tau_{LE}^+$  and  $\tau_{LE}^-$ . Note, however,  $L_H$ 's equivalent-series resistance (ESR) is parasitic and must therefore remain negligibly low to minimize the timing error and harvesting-performance degradation it produces.

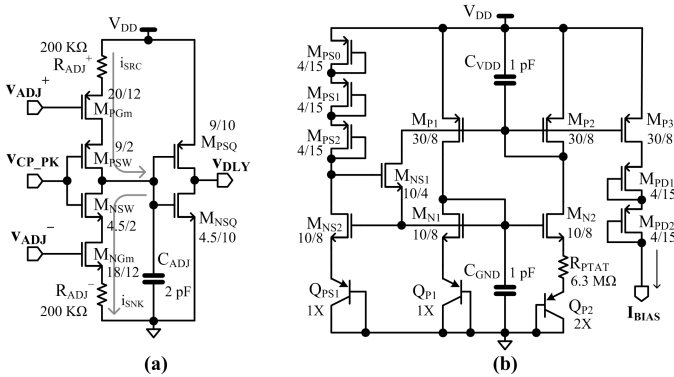


Fig. 9. (a) Adjustable delay  $\tau_{DLY}$  and (b) PTAT current-generator circuits (dimensions are in  $\mu\text{m}$  and body terminals connect to their respective supplies, unless otherwise specified).

The nanoamp generator shown in Fig. 9b biases  $CP_{PK}$ . Operationally, one-to-one mirror  $M_{P1}$ - $M_{P2}$  and gate-coupled pair  $M_{N1}$ - $M_{N2}$  ensure the  $M_{N1}$ - $M_{N2}$ 's source voltages equal. As a result, the area ratio between  $Q_{P2}$  and  $Q_{P1}$  establishes proportional-to-absolute-temperature (PTAT) diode-voltage difference  $\Delta V_D$  across  $R_{PTAT}$  to set  $I_{BIAS}$  to

$$I_{BIAS} = \frac{\Delta V_D}{R_{PTAT}} = \frac{V_t \ln\left(\frac{I_{P1} A_2}{I_{P2} A_1}\right)}{R_{PTAT}} = \frac{V_t \ln 2}{R_{PTAT}}, \quad (3)$$

which is supply independent. Here,  $V_t$  is the thermal voltage and  $I_{P1}$ - $I_{P2}$  and  $A_1$ - $A_2$  are  $Q_{P1}$ - $Q_{P2}$ 's currents and areas, respectively.  $R_{PTAT}$ 's large off-chip resistance (at 6.3 M $\Omega$ )

ensures  $I_{BIAS}$  is in the nanoamp range. Note  $I_{BIAS}$  is only PTAT if  $R_{PTAT}$  has a low temperature coefficient, which is not a requirement for this circuit. Without start-up transistor  $M_{NS1}$ , the circuit is stable at either the above-defined  $I_{BIAS}$  or zero, when  $M_{P1}$ - $M_{P2}$  is off and  $Q_{P1}$ - $Q_{P2}$ 's voltages are zero.  $M_{NS1}$  forces the circuit into its on state because  $M_{NS1}$ 's gate-source voltage would otherwise be high enough (as defined by  $M_{PS0}$ ,  $M_{PS1}$ ,  $M_{PS2}$ ,  $M_{NS2}$ , and  $Q_{PS1}$ ) to steer current from  $M_{P1}$  into  $M_{N1}$ . Incidentally, diode-connected PMOS transistors  $M_{PD1}$  and  $M_{PD2}$  level-shift  $CP_{PK}$ 's current-bias terminal voltage (across  $M_{NB}$  in Fig. 8) to decrease channel-length modulation errors in  $M_{P3}$ .

#### IV. CHARGING AND EFFICIENCY PERFORMANCE

Fig. 10a illustrates the fabricated  $940 \times 960\text{-}\mu\text{m}^2$  2- $\mu\text{m}$  BiCMOS IC and its corresponding printed-circuit-board (PCB) prototype. The measured inductance and ESR of the  $4.4 \times 4.4 \times 1.4\text{-mm}^3$  Coilcraft LPS4414 inductor were 160  $\mu\text{H}$  and 3.4  $\Omega$ . The Brüel & Kjær's Mini-Shaker 4810 shown in Fig. 10b generated the 100-Hz periodic vibrations used to stimulate the  $44 \times 13 \times 0.4\text{-mm}^3$  piezoelectric cantilever at its resonant frequency. A laser-displacement sensor measured the vertical position of the cantilever to study the relationship between mechanical and electrical parameters. The amplitude of the transducer's open-circuit voltage  $\Delta v_{PZT(\text{UNLOADED})}$  and the cantilever's acceleration rate rise almost linearly with shaker-vibration strength. For example,  $\Delta v_{PZT(\text{UNLOADED})}$  is 0.35, 0.5, 0.7, and 0.9 V when the acceleration at the base of the cantilever is 0.048, 0.069, 0.094, and 0.120  $\text{m/s}^2$  and at the tip of the cantilever is 3.05, 4.49, 6.44, and 8.34  $\text{m/s}^2$ , respectively.

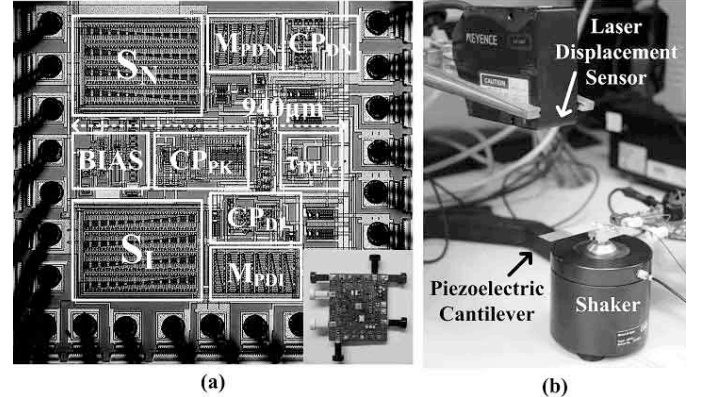


Fig. 10. (a) Die and PCB (inset), and (b) test setup of the prototyped harvester.

##### A. Charging Performance

The prototype successfully charged 160-nF SMD ceramic and 23- $\mu\text{F}$  electrolytic capacitors from inputs with  $\Delta v_{PZT(\text{UNLOADED})}$ 's of 0.35, 0.5, 0.7, and 0.9 V at successively increasing rates, as Fig. 11 shows. The capacitor voltages rise in staircase fashion because the circuit deposits a small, but fixed amount of energy (from  $CP_{ZT}$ ) every half cycle, much like a (trickle) pulse charger [32]–[34]. As expected, the resulting step size is smaller for 23  $\mu\text{F}$  and increases with larger  $\Delta v_{PZT(\text{UNLOADED})}$ 's because stronger mechanical vibrations deposit more energy into  $CP_{ZT}$ .

Energy per cycle (i.e., step size) is low (and charge time relatively long) because miniaturized harvesters produce little power. As such, the 1.2- and 1.5-mAh Li-Ion batteries in Fig. 12 (i.e., ML414 and VL621) charged from 0.65- and 0.9-V  $\Delta v_{PZT(UNLOADED)}$ 's to raise their corresponding voltages by 24 and 39 mV in 300 minutes. For these capacitor and battery charging experiments, an external low-leakage operational amplifier in unity-gain configuration monitored  $V_{BAT}$  and a low-leakage off-chip diode connected to an external 4-V supply clamped  $V_{BAT}$  within the targeted range.

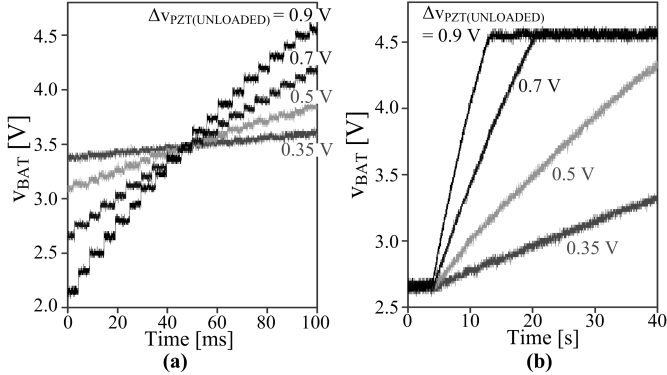


Fig. 11. Experimental time-domain charging profiles for (a) 160-nF SMD ceramic and (b) 23- $\mu$ F electrolytic capacitors.

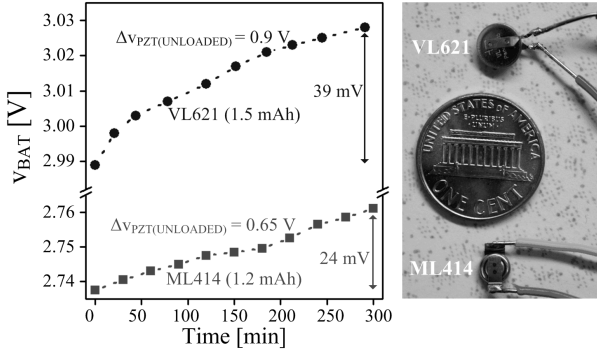


Fig. 12. Experimental time-domain charging profiles for Li-Ion batteries ML414 and VL621.

### B. Conversion Efficiency

After discounting losses, the system harnesses up to 30  $\mu$ W ( $P_H$  in Fig. 13) from 72  $\mu$ W of transducer-generated power ( $P_{IN(LOADED)}$ ). Without the harvester (i.e., unloaded) and under equal mechanical stimulation, energy per cycle in  $C_{PZT}$  (i.e.,  $C_{PZT}\Delta v_{PZT(UNLOADED)}^2 f_{VIB}$ ) can generate less power ( $P_{IN(UNLOADED)}$ ) than when loaded (e.g., 40 versus 72  $\mu$ W). This results, as expected, because extracting all  $C_{PZT}$ 's positive- and negative-cycle energy resets (i.e., conditions)  $v_{PZT}$  to zero, further increasing the transducer's electrical damping force and thereby inducing it to derive more energy from the environment. Note  $P_{IN(UNLOADED)}$  also represents the maximum input power a rectifier-based circuit can produce because a rectifier draws charge from  $C_{PZT}$  without conditioning its voltage. In other words, the best possible (and ideal) rectifier-based system would draw roughly 56% of what the proposed harvester can (e.g., 40 of 72  $\mu$ W).

Although increasing the transducer's output power by up to 78% or 1.78 $\times$  (when  $\Delta v_{PZT(UNLOADED)}$  is 1.2 V) by loading it

with the prototyped harvester corroborates theory, Eq. (2) predicts a 4 $\times$  (i.e., 400%) improvement. One reason for this discrepancy is  $C_{PK}$ 's 36-mV input-referred offset causes the system to discharge  $C_{PZT}$  past  $v_{PZT}$ 's peak, as already mentioned and shown in Fig. 4, after  $C_{PZT}$  loses some energy to vibrations. What is more, since the offset voltage does not scale with the input, the fraction of energy lost to vibrations is larger for smaller inputs, so loaded-to-unloaded input-power ratio  $P_{IN(LOADED)}/P_{IN(UNLOADED)}$  decreases from 1.78 rapidly (i.e., nonlinearly) with respect to  $\Delta v_{PZT(UNLOADED)}$ . Parasitic resistances in switches  $S_N$  and  $S_I$  and across  $L_H$  (in Figs. 3 and 5) also reduce the transducer's output power because, instead of fully draining  $C_{PZT}$  into  $L_H$  by lowering  $v_{PZT}$  to zero, the converter pulls  $v_{PZT}$  to the voltage drop across  $S_N$ ,  $L_H$ , and  $S_I$ 's combined series resistance  $R_{SN} + R_{ESR} + R_{SI}$ . This non-zero voltage not only represents remnant energy that the system does not harvest but also lowers the peak amplitude (i.e., electrical damping force) of the ensuing half cycle.

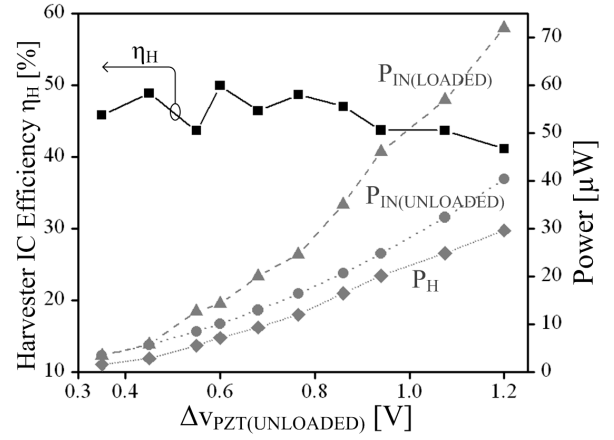


Fig. 13. Measured conversion efficiency  $\eta_H$ , input and output power  $P_{IN(LOADED)}$  and  $P_H$ , and unloaded input power  $P_{IN(UNLOADED)}$  across mechanical vibration strength (i.e., across  $C_{PZT}$ 's  $\Delta v_{PZT(UNLOADED)}$ ) at 100 Hz.

Ultimately, the harvesting conversion efficiency of the system with respect to  $P_{IN(LOADED)}$  ( $\eta_H$  in Fig. 13) across vibration strength falls between 40% and 50%. The system loses conduction energy  $E_C$  to the switches' finite resistances and  $L_H$ 's ESR when  $i_L$  flows through  $L_H$  during  $L_H$ 's positive- and negative-cycle energizing and de-energizing times  $\tau_{LE}^+$ ,  $\tau_{LDE}^+$ ,  $\tau_{LE}^-$ , and  $\tau_{LDE}^-$ . However, as Fig. 4 shows,  $L_H$  de-energizes in considerably less time than it energizes (i.e.,  $\tau_{LE}^+$  and  $\tau_{LE}^-$  are considerably longer than  $\tau_{LDE}^+$  and  $\tau_{LDE}^-$ ) so  $E_C$  mostly consists of energizing losses:

$$E_C \approx E_{C(LE)} \approx \left[ \left( \frac{I_{L(PK)}^+}{\sqrt{3}} \right)^2 + \left( \frac{I_{L(PK)}^-}{\sqrt{3}} \right)^2 \right] (R_{SI} + R_{SN} + R_{ESR}) \tau_{LE}^+ \quad (4)$$

where energizing times  $\tau_{LE}^+$  and  $\tau_{LE}^-$  equal (to  $\tau_{LE}$ ) and  $I_{L(PK)}^+/\sqrt{3}$  and  $I_{L(PK)}^-/\sqrt{3}$  are the root-mean-squared (RMS) currents flowing through the resistors across  $\tau_{LE}^+$  and  $\tau_{LE}^-$ , respectively.  $E_C$  falls with increasing  $L_H$  values because, even though  $\tau_{LE}$  increases with  $L_H^{0.5}$  (from  $1/2\pi\sqrt{L_H C_{PZT}}$ ),  $(I_{L(PK)}^+)^2$  and  $(I_{L(PK)}^-)^2$  decrease with  $L_H^{-1}$ . Wider MOS transistors (i.e., lower  $R_{SI}$  and  $R_{SN}$ ) also decrease  $E_C$ , but at the expense of silicon real estate and higher switching gate-drive losses  $E_{SW(GD)}$ , as the following discussion will elucidate.

The system loses  $E_{SW(GD)}$  in inverter drivers when they charge and discharge parasitic gate capacitances in  $S_I$ ,  $S_N$ , and  $D_N$  and  $D_I$ 's  $M_{PDN}$  and  $M_{PDI}$  (from Fig. 5). Since all the switches in the proposed harvester engage and disengage once per cycle, gate-drive losses amount to

$$E_{SW(GD)} \approx (C_{SI} + C_{DI} + C_{DN})V_{DD}^2 + C_{SN}(V_{DD} + |V_{PZT(PK)}^-|)^2, \quad (5)$$

where  $C_{SI}$ ,  $C_{DI}$ ,  $C_{DN}$ , and  $C_{SN}$  refer to the parasitic capacitances that  $S_I$ ,  $D_I$ 's  $M_{PDI}$ ,  $D_N$ 's  $M_{PDN}$ , and  $S_N$  introduce, respectively, which scale with transistor channel widths. Note  $S_N$  causes more energy loss than other switches because its gate swings between  $V_{DD}$  and  $V_{PZT(PK)}^-$ .

The system also loses overlap losses  $E_{SW(IV)}$  when MOS drain currents and drain-source voltages shortly overlap every time they transition. In the prototyped system, this overlap occurs when  $S_N$  and  $S_I$  open because  $v_{SW}^+$  and  $v_{SW}^-$  transition with a non-zero  $i_L$ :

$$E_{SW(IV)} \approx (0.5I_{L(PK)}^+ \tau_{SN\_OFF} + 0.5I_{L(PK)}^- \tau_{SI\_OFF})(V_{BAT} + V_D), \quad (6)$$

where  $V_D$  refers to  $M_{PDN}$  and  $M_{PDI}$ 's body-diode voltage. Here, because  $i_L$  is triangular and  $\tau_{SN\_OFF}$  and  $\tau_{SI\_OFF}$  are  $S_N$  and  $S_I$ 's corresponding off times,  $0.5I_{L(PK)}^+ \tau_{SN\_OFF}$  and  $0.5I_{L(PK)}^- \tau_{SI\_OFF}$  represent  $S_N$  and  $S_I$ 's total conducted charge during transitions.

Peak-detector comparator  $CP_{PK}$ , the nanoamp-bias generator, adjustable delay block  $\tau_{ADJ}$ , the logic gates, and  $D_N$  and  $D_I$ 's comparators  $CP_{DN}$  and  $CP_{DI}$  in Fig. 5 also dissipate quiescent energy ( $E_Q$ ). The losses in  $CP_{PK}$  and the bias circuit, however, dominate  $E_Q$  because they operate through the entire vibration cycle, whereas the other circuits only engage for a substantially smaller fraction. Overall, although higher input power increases  $|V_{PZT(PK)}^-|$ ,  $I_{L(PK)}^+$ , and  $I_{L(PK)}^-$  and their associated switching losses  $E_{SW(GD)}$  and  $E_{SW(IV)}$ , conduction losses  $E_C$  scales more rapidly with power (i.e., proportional to  $(I_{L(PK)}^+)^2$  and  $(I_{L(PK)}^-)^2$ ) so  $E_C$  ultimately dominates and limits  $\eta_H$  when mechanical vibrations are strong. Conversely, when vibrations are weak,  $E_Q$  can dominate because  $E_C$ ,  $E_{SW(GD)}$ , and  $E_{SW(IV)}$  scale with power. Similarly,  $E_Q$  can also dominate when the frequency of the input vibration is low because, since the harvester synchronizes itself to a lower vibration period,  $E_C$ ,  $E_{SW(GD)}$ , and  $E_{SW(IV)}$  decrease accordingly. A fundamental challenge here is that  $E_Q$  remains constant so  $\eta_H$  degrades with decreasing strength and vibrations.

The increase in  $\eta_H$  with decreasing vibration strength (i.e.,  $\Delta V_{PZT(UNLOADED)}$ 's) across the upper half of the tested range (in Fig. 13) indicates conduction losses  $E_C$  dominate because  $E_C$  scales more rapidly with strength than output power  $P_H$  does. Through the lower range,  $\eta_H$  is for the most part even, which implies switching losses  $E_{SW(GD)}$  and  $E_{SW(IV)}$  overwhelm other losses in that region because linear reductions in  $E_{SW(GD)}$  and  $E_{SW(IV)}$  offset (and balance) linear drops in  $P_H$ . Since  $\eta_H$  does not fall noticeably with decreasing mechanical strength, quiescent losses  $E_Q$  do not appear to dominate. Given all this, increasing  $\eta_H$  in the upper range is possible by increasing  $S_I$  and  $S_N$ 's channel widths (i.e., decreasing their corresponding resistances) because  $E_C$  would decline more than  $E_{SW(GD)}$  would increase.

## V. PERFORMANCE UNDER PRACTICAL OPERATING CONDITIONS

Vibrations in practical operating environments occur, for the most part, at relatively low frequencies, between maybe 1 Hz for a person walking to 167 Hz for an engine cycling at 10,000 revolutions per minute. What is more, the rate is often inconsistent and maybe even non-recurring, as in the case of human motion, wind-propelled movements, and vibrations generated from impact [35]. What all this means is that matching the narrow band of a transducer to vibrations, which is the recipe for high conversion efficiency, is oftentimes impractical and unrealistic.

Because the prototyped harvester automatically detects when to draw energy from  $C_{PZT}$ , the proposed system is capable of harnessing energy from non-periodic stimuli. When dropping a 145-g official major-league baseball from 40 cm above the experimental setup table in Fig. 10b, for example, the impact of the ball bouncing once off the table induces the piezoelectric cantilever to vibrate and produce the pulse train in Fig. 14a-b. In this case, the prototyped system charged 500 nF (from 3.04 V) from a single bounce for three separate trials by roughly 200 mV.

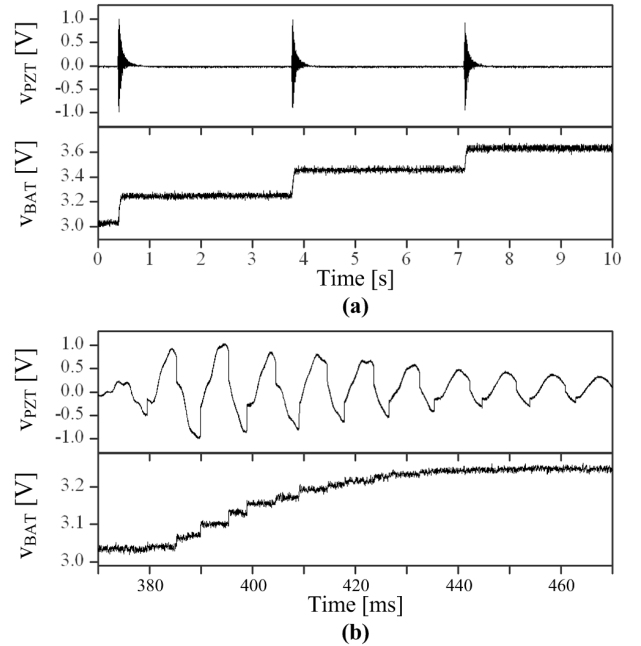


Fig. 14. (a) Second and (b) millisecond (magnified) responses to the impact of a baseball bouncing off a table.

Each drop produces the decaying vibrations Fig. 14b illustrates where the system harvests energy by quickly draining  $C_{PZT}$  into  $L_H$  and then  $L_H$  into the 500-nF capacitor each time  $v_{PZT}$  peaks. As  $v_{PZT}$ 's peaks (and mechanical strength) decrease, however, peak-detector comparator  $CP_{PK}$ 's offset has a larger impact on how much input power  $P_{IN(LOADED)}$  the system harnesses so output power  $P_H$  decreases more than basic theory predicts. Under these weak vibrations, in fact,  $R_D-C_D$  and  $CP_{PK}$ 's delays increase  $CP_{PK}$ 's offset to degrade performance. In contrast, just as  $CP_{PK}$ 's offset *adds* to the effects of  $CP_{PK}$ 's delay in the positive half-cycle, the offset  *cancels*  delay in the negative half-cycle, as Figs. 4 and 14b

indicate, which means alternating the polarity of the offset can improve overall performance.

Although the immediate aim of this research is to raise  $P_H$  by increasing  $\eta_H$  and  $P_{IN(LOADED)}$ , the ultimate metric is end-to-end harvesting conversion efficiency  $\eta_{TOTAL}$ , which refers to how much mechanical energy  $E_{ME}$  reaches the output as harvested energy  $E_H$ . A means of applying a known value for  $E_{ME}$  (and approximating  $\eta_{TOTAL}$ ) is to tie an object of known mass  $m_W$  to the tip of the piezoelectric cantilever with a light string and subsequently cut the link. Since the cantilever's elastic force  $F_C$  balances the object's gravitational pull  $F_G$ ,  $E_{ME}$  relates to  $F_G$  and the cantilever's tip displacement distance  $d_C$ :

$$E_{ME} = \frac{K_C d_C^2}{2} = \frac{(K_C d_C) d_C}{2} = \frac{F_C d_C}{2} = \frac{F_G d_C}{2} = \frac{(m_W g) d_C}{2}, \quad (7)$$

where  $K_C$  and  $g$  refer to the spring constant and gravity's acceleration, respectively.

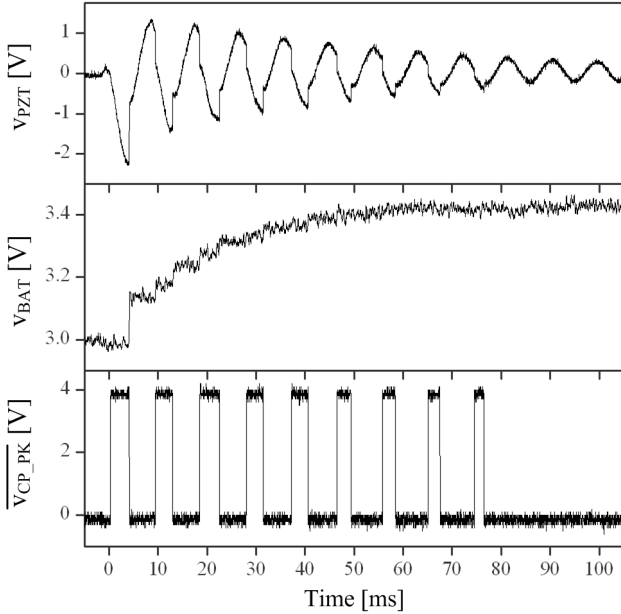


Fig. 15. End-to-end harvesting waveforms for a 3-g weight.

This way, neglecting parasitic weights and assuming the string severs instantaneously, the prototyped harvester charged (experimentally) 500 nF by roughly 400 mV, as Fig. 15 shows, from a 3-g weight. As a result, subtracting the external supply's quiescent energy  $E_Q$  (to the chip for  $CP_{PK}$ , bias generator, adjustable delay, and logic gates) and gate-driving losses  $E_{SW(GD)}$  from the energy deposited in the 500-nF capacitor reduces  $E_H$  to

$$E_H = 0.5C_{BAT} (V_{BAT(F)}^2 - V_{BAT(I)}^2) - E_Q - E_{SW(GD)}, \quad (8)$$

which ranged between 100 and 660 nJ when stimulated with 1.2 to 10.8  $\mu J$  of  $E_{ME}$  from 1-, 2-, and 3-g weights to yield  $6.1 \pm 1.5\%$  to  $8.8 \pm 6.9\%$  of  $\eta_{TOTAL}$  or  $E_H/E_{ME}$ . Table I summarizes the statistical results (mean and standard deviation) for each weight across 20 trials. To minimize the mechanical disturbance that cutting the link creates, Table I considers only data whose initial peak voltage ( $v_{PZT}$ ) was small (e.g., less than 100 mV), like Fig. 15's  $v_{PZT}$ .

$\eta_{TOTAL}$  incorporates the collective performance of the transducer ( $\eta_{PZT(LOADED)}$ ) and the harvester ( $\eta_H$ ), which means  $\eta_{PZT(LOADED)}$  is  $\eta_{TOTAL}/\eta_H$  or roughly 14% – 20% when assuming (from Fig. 13)  $\eta_H$  is 45% on average. Since  $\eta_{PZT(LOADED)}$  includes a factor improvement the harvester induces, the unloaded counterpart ( $\eta_{PZT(UNLOADED)}$ ) is less than 14% – 20% by up to 1.78 $\times$ . Although this simple analysis is by no means accurate or complete, it shows that mechanical losses are significant at around 80% and conditioning the transducer to increase  $P_{IN(LOADED)}$  is as important as reducing the losses across the switched-inductor converter (i.e., increasing  $\eta_H$ ).

TABLE I  
MEASURED MECHANICAL AND NET HARVESTED ENERGY, AND END-TO-END EFFICIENCIES

Weight [g]	$E_{ME}$ [nJ]	$E_H$ [nJ]	$\eta_{TOTAL}$ [%]
1	$1198.0 \pm 17.6$	$104.8 \pm 82.3$	$8.76 \pm 6.89$
2	$4797.0 \pm 123.1$	$402.8 \pm 173.3$	$8.39 \pm 3.60$
3	$10792.8 \pm 190.3$	$659.1 \pm 171.2$	$6.10 \pm 1.54$

## VI. CONCLUSIONS

The prototyped 2- $\mu m$  BiCMOS switched-inductor piezoelectric harvester developed, experimentally evaluated, and presented in this paper generates and steers up to 30  $\mu W$  from a periodic 72- $\mu W$  piezoelectric source into a capacitor or battery directly. In doing so, it increases the piezoelectric cantilever's electrical damping force to raise the transducer's (and therefore system's end-to-end) mechanical-electrical efficiency by up to 78%. The system also harnesses up to 659 nJ from non-periodic vibrations with  $6.1 \pm 1.5\%$  to  $8.8 \pm 6.9\%$  end-to-end mechanical-electrical efficiencies. One key feature of the presented harvester is that it eliminates the need for a rectifier. As a result, the system no longer (i) places a threshold limit imposed by diodes and/or the output voltage on mechanical vibrations, (ii) loses power across an otherwise additional stage (i.e., across a rectifier), and (iii) limits how much the circuit dampens the transducer (to produce more power). Conditioning the piezoelectric device to generate more power is an important attribute, as is the relatively simple and low-loss control strategy the system adopts to energize and de-energize the inductor directly into the energy-storage device. From a practical standpoint, the harvester is also able to harness energy from short, non-periodic mechanical vibrations, which are more prevalent in real-life applications, such as when someone jumps or suddenly stops, wind gushes, objects crash, and so on.

## VII. ACKNOWLEDGMENT

The authors thank Linear Technology Corporation for sponsoring this research and fabricating the prototyped IC and Bryan Legates and his team for their advice and encouragement.

## REFERENCES

- [1] D.A. La Van, T. McGuire, and R. Langer, "Small-scale systems for in vivo drug delivery," *Nature Biotechnology*, vol. 21, no. 10, pp. 1184–1191, Oct. 2003.

- [2] J. Marek, "MEMS for automotive and consumer electronics," in *IEEE Int. Solid-State Circuits Conf. (ISSCC) Dig. Tech. Papers*, Feb. 2010, vol. 53, pp. 9–17.
- [3] M. Flatscher, M. Dielacher, T. Herndl, T. Lentsch, R. Matischek, J. Prainsack, W. Pribyl, H. Theuss, and W. Weber, "A bulk acoustic wave (BAW) based transceiver for an in-tire-pressure monitoring sensor node," *IEEE J. Solid-State Circuits*, vol. 45, no. 1, pp. 167–177, Jan. 2010.
- [4] J. Yoo, L. Yan, S. Lee, Y. Kim, and H.-J. Yoo, "A 5.2 mW self-configured wearable body sensor network controller and a 12  $\mu$ W wirelessly powered sensor for a continuous health monitoring system," *IEEE J. Solid-State Circuits*, vol. 45, no. 1, pp. 178–188, Jan. 2010.
- [5] I.F. Akyildiz, W. Su, Y. Sankarasubramaniam, and E. Cayirci, "Wireless sensor networks: a survey," *Computer Networks*, vol. 38, pp. 393–422, 2002.
- [6] N.J. Guilar, T.J. Kleeburg, A. Chen, D.R. Yankelevich, and R. Amirtharajah, "Integrated solar energy harvesting and storage," *IEEE Trans. VLSI Syst.*, vol. 17, no. 5, pp. 627–637, May 2009.
- [7] H. Lhermet, C. Condemine, M. Plissonnier, R. Salot, P. Audebert, and M. Rosset, "Efficient power management circuit: from thermal energy harvesting to above-IC microbattery energy storage," *IEEE J. Solid-State Circuits*, vol. 43, no. 1, pp. 246–255, Jan. 2008.
- [8] E.J. Carlson, K. Strunz, and B.P. Otis, "A 20 mV input boost converter with efficient digital control for thermoelectric energy harvesting," *IEEE J. Solid-State Circuits*, vol. 45, no. 4, pp. 741–750, Apr. 2010.
- [9] T. Le, K. Mayaram, and T. Fiez, "Efficient far-field radio frequency energy harvesting for passively powered sensor networks," *IEEE J. Solid-State Circuits*, vol. 43, no. 5, pp. 1287–1302, May 2008.
- [10] J.A. Paradiso and T. Starner, "Energy scavenging for mobile and wireless electronics," *Pervasive Computing*, vol. 4, pp. 18–27, 2005.
- [11] P.D. Mitcheson, E.M. Yeatman, G.K. Rao, A.S. Holmes, and T.C. Green, "Energy harvesting from human and machine motion for wireless electronic devices," *Proceedings of the IEEE*, vol. 96, no. 9, pp. 1457–1486, Sept. 2008.
- [12] S. Roundy, P.K. Wright, and J. Rabaey, "A study of low level vibrations as a power source for wireless sensor nodes," *Computer Communications*, vol. 26, pp. 1131–1144, 2003.
- [13] S. Priya and D.J. Inman, *Energy Harvesting Technologies*, New York, NY: Springer Science+Business Media, LLC 2009.
- [14] T.T. Le, J. Han, A. von Jouanne, K. Mayaram, and T.S. Fiez, "Piezoelectric micro-power generation interface circuits," *IEEE J. Solid-State Circuits*, vol. 41, no. 6, pp. 1411–1420, June 2006.
- [15] N.J. Guilar, R. Amirtharajah, and P.J. Hurst, "A full-wave rectifier with integrated peak selection for multiple electrode piezoelectric energy harvesters," *IEEE J. Solid-State Circuits*, vol. 44, no. 1, pp. 240–246, Jan. 2009.
- [16] D. Guyomar, A. Badel, E. Lefeuvre, and C. Richard, "Toward energy harvesting using active materials and conversion improvement by nonlinear processing," *IEEE Trans. Ultrasonics, Ferroelectrics, and Frequency Control*, vol. 52, no. 4, pp. 584–595, Apr. 2005.
- [17] E. Lefeuvre, A. Badel, C. Richard, and D. Guyomar, "Piezoelectric energy harvesting device optimization by synchronous electric charge extraction," *J. Intelligent Material Systems and Structures*, vol. 16, pp. 865–876, Oct. 2005.
- [18] A. Badel, D. Guyomar, E. Lefeuvre, and C. Richard, "Piezoelectric energy harvesting using a synchronized switch technique," *J. Intelligent Material Systems and Structures*, vol. 17, pp. 831–839, Aug./Sept. 2006.
- [19] M. Lallart, L. Garbuio, C. Richard, and D. Guyomar, "Low-cost capacitor voltage inverter for outstanding performance in piezoelectric energy harvesting," *IEEE Trans. Ultrasonics, Ferroelectrics, and Frequency Control*, vol. 57, no. 2, pp. 281–291, Feb. 2010.
- [20] Y.K. Ramadass and A.P. Chandrakasan, "An efficient piezoelectric energy harvesting interface circuit using a bias-flip rectifier and shared inductor," *IEEE J. Solid-State Circuits*, vol. 45, no. 1, pp. 189–204, Jan. 2010.
- [21] G.K. Ottman, H.F. Hofmann, A.C. Bhatt, and G.A. Lesieutre, "Adaptive piezoelectric energy harvesting circuit for wireless remote power supply," *IEEE Trans. Power Electronics*, vol. 17, no. 5, pp. 669–676, Sept. 2002.
- [22] G.K. Ottman, H.F. Hofmann, and G.A. Lesieutre, "Optimized piezoelectric energy harvesting circuit using step-down converter in discontinuous conduction mode," *IEEE Trans. Power Electronics*, vol. 18, no. 2, pp. 696–703, March 2003.
- [23] W.J. Choi, Y. Jeon, J.-H. Jeong, R. Sood, and S.G. Kim, "Energy harvesting MEMS device based on thin film piezoelectric cantilevers," *J. Electroceram.*, vol. 17, pp. 543–548, 2006.
- [24] M. Renaud, K. Karakaya, T. Sterken, P. Fiorini, C. Van Hoof, and R. Puers, "Fabrication, modelling and characterization of MEMS piezoelectric vibration harvesters," *Sensors and Actuators A (Physical)*, vol. 145–146, pp. 380–386, July–Aug. 2008.
- [25] N.M. White, P. Glynne-Jones, and S.P. Beeby, "A novel thick-film piezoelectric micro-generator," *Smart Mater. Struct.*, vol. 10, pp. 850–852, 2001.
- [26] B.-S. Lee, S.-C. Lin, and W.-J. Wu, "Comparison of the piezoelectric MEMS generators with interdigital electrodes and laminated electrodes," in *Proceedings of the SPIE-The International Society for Optical Engineering*, March 2008, pp. 69331B-1–69331B-8.
- [27] D. Kwon and G.A. Rincón-Mora, "A rectifier-free piezoelectric energy harvester circuit," in *Proc. IEEE Int. Symp. Circuits and Systems (ISCAS)*, May 2009, pp. 1085–1088.
- [28] D. Kwon and G.A. Rincón-Mora, "A single-inductor AC-DC piezoelectric energy-harvester/battery-charger IC converting  $\pm(0.35$  to  $1.2V)$  to  $(2.7$  to  $4.5V)$ ," in *IEEE Int. Solid-State Circuits Conf. (ISSCC) Dig. Tech. Papers*, Feb. 2010, vol. 53, pp. 494–495.
- [29] T.Y. Man, P.K.T. Mok, and M.J. Chan, "A 0.9-V input discontinuous-conduction-mode boost converter with CMOS-control rectifier," *IEEE J. Solid-State Circuits*, vol. 43, no. 9, pp. 2036–2046, Sept. 2008.
- [30] Y.-H. Lam, W.-H. Ki, and C.-Y. Tsui, "Integrated low-loss CMOS active rectifier for wirelessly powered devices," *IEEE Trans. Circuits Syst. II*, vol. 53, no. 12, pp. 1378–1382, Dec. 2006.
- [31] S. Guo, and H. Lee, "An efficiency-enhanced CMOS rectifier with unbalanced-biased comparators for transcutaneous-powered high-current implants," *IEEE J. Solid-State Circuits*, vol. 44, no. 6, pp. 1796–1804, June 2009.
- [32] J. Li, E. Murphy, J. Winnick, and P.A. Kohl, "The effects of pulse charging on cycling characteristics of commercial lithium-ion batteries," *J. Power Sources*, vol. 102, pp. 302–309, 2001.
- [33] Z. Jiang, and R.A. Dougal, "Synergetic control of power converters for pulse current charging of advanced batteries from a fuel cell power source," *IEEE Trans. Power Electronics*, vol. 19, no. 4, pp. 1140–1150, July 2004.
- [34] L.-R. Chen, "A design of an optimal battery pulse charge system by frequency-varied technique," *IEEE Trans. Industrial Electronics*, vol. 54, no. 1, pp. 398–405, Feb. 2007.
- [35] F. Cottone, H. Vocca, and L. Gammaitoni, "Nonlinear energy harvesting," *Physical Review Lett.*, vol. 102, pp. 080601-1–4, Feb. 2009.



**Dongwon Kwon** (S'07) received the B.S. degree from Seoul National University and the M.S.E.E. degree from Georgia Institute of Technology in 2003 and 2008, respectively, all in electrical engineering. From 2003 to 2006, he worked as a research engineer in Hantel Inc., Kyunggi, Korea and developed portable MP3 players. He has been working toward his Ph.D. degree in Georgia Tech Analog, Power, and Energy IC Lab since spring 2007. His research interests include piezoelectric energy harvesting circuits, switching-mode power ICs, and ultra-low-power analog IC design. He won the 2<sup>nd</sup> place in the 2009 Science Applications International Corporation-Georgia Tech student paper competition.



**Gabriel A. Rincón-Mora** (S'91-M'97-SM'01) received his B.S., M.S., and Ph.D. in electrical engineering and worked for Texas Instruments in '94-'03, was appointed Adjunct Professor for Georgia Tech in '99-'01, and became a full-time faculty member at Georgia Tech in '01. His scholarly products include 8 books, 1 book chapter, over 125 scientific publications, 27 patents, over 26 commercial chip designs, and over 55 international speaking engagements. He received the "National Hispanic in Technology Award," "Charles E. Perry Visionary Award," a "Commendation Certificate" from the Lieutenant Governor of California, IEEE CASS Service Award, and Robins Air Force Base's "Orgullo Hispano" and "Hispanic Heritage" awards. He was elevated to the grade of Fellow by IET, inducted into Georgia Tech's "Council of Outstanding Young Engineering Alumni," elected IEEE CASS Distinguished Lecturer for '09-'10,

and featured on the cover of Hispanic Business magazine as one of "The 100 Most Influential Hispanics." He is Associate Editor for IEEE's TCAS II (since '08); Editorial Board Member for JOLPE (since 2009); Chairman of Atlanta's IEEE SSCS-CASS Chapter (since '05); Technical Committee Member for IEEE's CASS ASP and PECAS; Steering Committee Member for IEEE's MWSCAS; was General Chair for SRC's Energy and Power ICs Workshop in '09; Circuit Design Vice Chair for IEEE's '08 ICCDCS; Technical Program Chair for IEEE's '07 MWSCAS-NEWCAS; Technical Program Co-Chair for IEEE's '06 MWSCAS; and Vice Chairman of Atlanta's SSCS-CASS Chapter in '04.